NANO · MICRO small
www.small-journal.com

# Hydrothermal Coating of Patterned Carbon Nanotube Forest for Structured Lithium-Ion Battery Electrodes

*Sarah Jessl, Davor Copic, Simon Engelke, Shahab Ahmad, and Michael De Volder**

**Controlling the arrangement and interface of nanoparticles is essential to achieve good transfer of charge, heat, or mechanical load. This is particularly challenging in systems requiring hybrid nanoparticle mixtures such as combinations of organic and inorganic materials. This work presents a process to coat vertically aligned carbon nanotube (CNT) forests with metal oxide nanoparticles using microwave-assisted hydrothermal synthesis. Hydrothermal processes normally damage delicate CNT forests, which is addressed here by a combination of lithographic patterning, transfer printing, and reduction of the synthesis time. This process is applied for the fabrication of structured Li-ion battery (LIB) electrodes where the aligned CNTs provide a straight electron transport path through the electrode and the hydrothermal coating process is used to coat the CNTs with conversion anode materials for LIBs. These nanoparticles are anchored on the surface of the CNTs and batteries fabricated following this process show a fourfold longer cyclability. Finally, this process is used to create thick electrodes (350 µm) with a gravimetric capacity of over 900 mAh $g^{-1}$.**

## 1. Introduction

Because of the large surface area of nanoparticles, controlling the interface between nanoparticles and their surroundings is important for most nanotechnology applications. This is particularly true for applications that require hybrid nanomaterial mixtures (e.g., organic and inorganic) and require good electron transport between both materials. For instance, in Li-ion battery (LIB) electrodes, a conductive additive (often carbon nanoparticles), and active battery materials are mixed and controlling electron transfer between these materials is important for the battery performance. Previous studies have shown that synthesizing the active material directly on the surface of the conductive additive enhances electron transport and allows, for instance, to drastically improve the battery lifetime.[1–11] In addition to controlling the material interface, the long-range order of nanomaterials in battery electrodes is important to control the electron transport, as well as the electrode tortuosity to improve Li-ion transport. This can, for instance, be achieved by vertically aligned carbon nanotube (VACNT) "forests," which are interesting conductive backbones for battery electrodes as they are electrochemically stable and provide a direct electrical wiring perpendicular to the current collectors.[12,13] In addition, techniques are available to organize CNTs in high aspect ratio structures[12–18] and to shape them in various forms,[19–21] which allows to create, for instance, thick Si LIB anodes[7] and flexible batteries.[22–25]

While the above advances are impressive, the current coating methods for VACNT forests are mainly based on gas phase processes (e.g., chemical vapor deposition of Si) in order not to damage these fragile structures,[18] which limits the battery chemistries that can be used. Alternatively, active battery particle suspensions have been drop-casted on VACNT forests,[21,26,27] but this requires attention to the stability of the CNT forest,[21] and because this does not result in good interfaces between both materials; this often leads to shorter lifetimes.[1–11] To address this challenge, we developed a protocol that allows for hydrothermal coating of metal oxide nanoparticles ($\alpha$-$Fe_2O_3$-nanoflakes) directly on patterned CNT forest without damaging the VACNT structures.[22,28–32] To the best of our knowledge, one-step hydrothermal synthesis has not been used to decorate patterned VACNT forests for battery electrodes previously as this process tends to destroy VACNT structures (see further).

**Figure 1**A shows the difference in electrode morphology between a classic battery slurry (Figure 1A left), and the structured VACNT honeycomb architecture proposed in this work (Figure 1A right). The latter offers (i) an efficient electron transport from active material to the Cu current collector through the vertically aligned CNT backbone; (ii) a robust high surface area electrode for high areal mass loading of active material; (iii) an open structure for efficient Li-ion transport; and (iv) a

S. Jessl, D. Copic, S. Engelke, S. Ahmad, M. De Volder
Department of Engineering
University of Cambridge
Cambridge CB2 1PZ, UK
E-mail: mfld2@cam.ac.uk
S. Engelke
Cambridge Graphene Centre
University of Cambridge
9 JJ Thomson Avenue, Cambridge CB3 0FA, UK
S. Ahmad[+]
Centre for Nanoscience and Nanotechnology
Jamia Millia Islamia (Central University)
New Delhi 110025, India
The ORCID identification number(s) for the author(s) of this article can be found under https://doi.org/10.1002/smll.201901201.



[+]Present address: Department of Physics, Indian Institute of Technology Jodhpur, Jodhpur 347032, India

**DOI: 10.1002/smll.201901201**

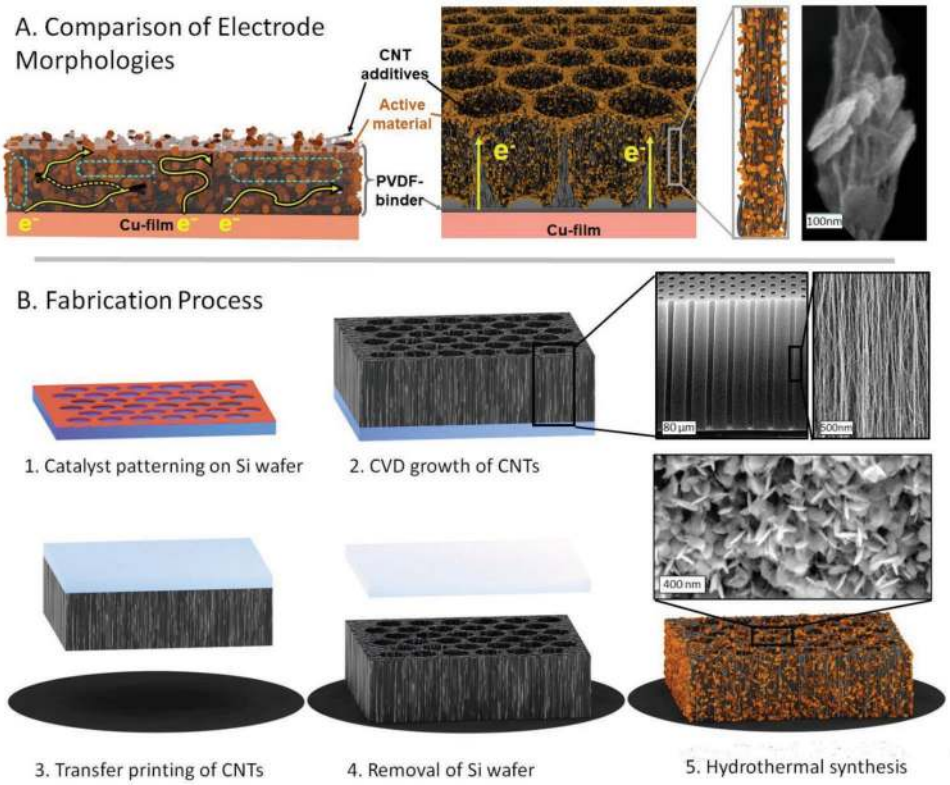


**Figure 1.** A) Comparison of the morphologies of a standard battery electrode (left) and our suggested electrode structure (right), which allows for better Li-ion and electron transport. B) Fabrication process of the electrodes using CVD growth of CNTs and hydrothermal synthesis of $\alpha$-$Fe_2O_3$ nanoplatelets.

good interface between the active material and the CNTs by the in situ hydrothermal synthesis for a long battery lifetime. A disadvantage of this new open electrode structure is that it has a lower volumetric density and requires more electrolyte, which can be expensive. However, we believe that the proposed honeycomb structure is interesting for applications such as on-chip batteries where a small footprint on the Si chip is more important than the volumetric or gravimetric performance. These microbatteries often have an porous architecture,[33] which requires more electrolyte. We believe this is justified by the fact that the fabrication cost of microbatteries is typically high compared to the electrolyte and because of their small size the amount of electrolyte is limited. Further work could look into reducing the honeycomb lattice size, as well as molding processes to fabricate these structures more cost-effectively.[34]

Hydrothermal coating of VACNTs is made possible in this work by: (i) patterning and oxidizing the VACNTs to allow for a good precursor access through the thickness of the electrodes. (ii) Using a transfer printing method that decouples the substrate on which the CNTs are synthesized and coated from the collector electrode material needed for the battery. In addition, this transfer printing process secures the CNTs firmly to the substrate during the synthesis and prevents delamination. (iii) Using a microwave synthesis process to reduce the reaction time and efficiently heat the CNTs.[35] (iv) Using a hydrothermal protocol that does not require a high temperature annealing step as this would decompose our transfer printing binder and possibly damage the CNTs (see further).

Overall, we anticipate that the above approach can be used to decorate aligned CNT structures with a variety of nanoparticles. Here, hematite was selected as an anode material to demonstrate this process. Hematite is interesting since it can be synthesized by a variety of well-documented methods;[29–32,36–41] moreover, it is cost effective and can store 1006 mAh $g^{-1}$ following a conversion reaction[31,40,42]

$$Fe_2O_3 + 6Li^+ \rightarrow 3Li_2O + 2Fe \quad (1)$$

Finally, because hematite nanoparticles are synthesized directly onto the CNT backbones, a binder is only needed locally at the base of the CNT structure to secure it on the Cu current collector foil (see Figure 1A right), which is advantageous compared to the standard battery electrodes, made from a slurry, which have binder throughout the electrode structure (see Figure 1A left). This allows to create thick electrodes (here 350 µm) where the top part of the battery is binder free to further enhance transport.[21,43] Electrochemical measurements show that our proposed electrode architecture allows for over a fourfold improvement in lifetime, combined with a twofold improvement in areal loading and excellent utilization of the active materials (gravimetric capacity of ≈912 mAh $g^{-1}$).

## 2. Fabrication and Synthesis Process

The fabrication process of the electrodes is illustrated in Figure 1B and detailed in the Experimental Section. First, a catalyst layer (10 nm $Al_2O_3$–1 nm Fe) is patterned using UV-lithography (see the Experimental Section, Figure 1B1). From

this catalyst layer, VACNTs are grown using a thermal chemical vapor deposition (CVD) protocol (see the Experimental Section, Figure 1B2). This structure is then microcontact transfer printed onto a conductive layer on a glass substrate, termed as PCP film, composed of poly(vinylidene fluoride) (PVDF) and conductive additives (CNTs and phenyl C61 butyric acid methyl ester (PCBM)), following a recipe previously reported[21] (Figure 1B3). This ≈15 µm thick film acts as a conductive and adhesive binder. Importantly, this film only infiltrates in the base of our 350 µm thick electrodes (Figure S3d, Supporting Information), which therefore operate mostly as a binder-free system. During the contact printing process the conductive PCP film is first placed on a hot-plate at 175 °C, the VACNT microstructures are then pushed onto the film and after cooling down to room temperature, the Si-wafer substrate is removed, leaving the CNT electrode strongly attached to the conductive film (Figure 1B4). Figure S1 (Supporting Information) shows that the capillary rise of the adhesive film in the CNT forest is only about 10 µm high. Next, the transfer-printed electrodes are treated with UV–ozone to oxidize the CNT walls and improve their wetting.[44,45] The electrodes are then loaded in a microwave-assisted hydrothermal reactor with an aqueous iron-sulfate precursor solution and are heated up to 165 °C for 6 h (Figure 1B5). Finally, the PCP film with these new decorated electrodes is peeled off the glass substrate and then assembled in half coin cells with a copper current collector and compared to reference electrodes using a slurry of CNT powders with active nanoparticles prepared by the same microwave hydrothermal synthesis method as well as CNT honeycomb structures with the same active particles drop-casted on the electrodes instead of being functionalized in situ.

## 3. Results and Discussion

**Figure 2**a,b shows the CNT scaffold before and after the microwave-assisted hydrothermal reaction. The aspect ratio of the pores is over 17, and their structure is maintained during the harsh hydrothermal processing conditions, with just a slight reshaping into a honeycomb-like structure due to capillary aggregation when drying the sample (close-ups in Figure S2, Supporting Information, and large-area images in Figure S3a–c, Supporting Information).[13,46–48] The height evolution of the structure during these processing steps is also shown in Figure S3d. The hydrothermal synthesis results in iron oxide nanoplatelets that are ≈150 nm wide and are anchored on the CNTs (Figure 1A and Figure S4, Supporting Information). X-ray diffraction (XRD) measurements of iron oxide particles formed during the hydrothermal synthesis in solution confirm they are hematite (see Figure 2c). All peaks were indexed and match well with the rhombohedral phase (R-3c space group), confirming that this one-step reaction can be used to obtain crystalline $Fe_2O_3$-platelets without thermal annealing directly on VACNT. This is important since annealing would decompose the PVDF-based conductive PCP film and potentially damage the CNTs. Raman spectroscopy before and after the above process (Figure 2d) shows that the G/D ratio of the CNTs decreases, as expected from the UV–ozone treatment,[44,49] and further the coated forests

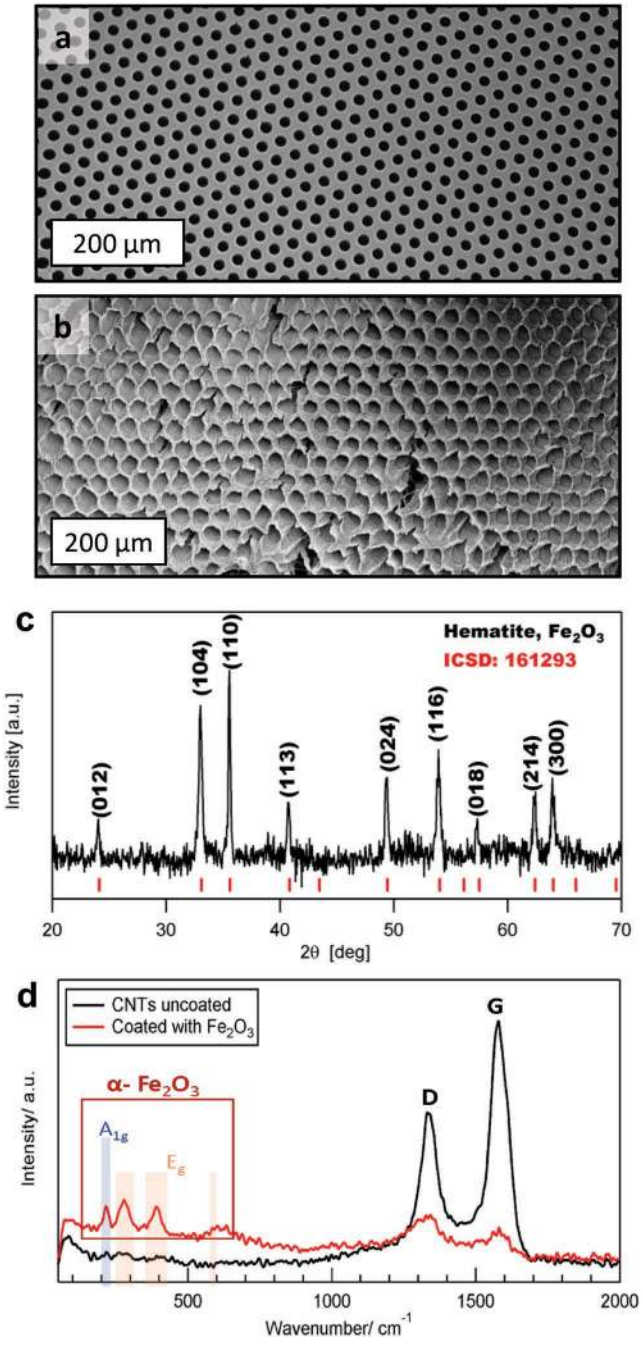


**Figure 2.** a,b) SEM images of the microstructured VACNTs before and after microwave-assisted hydrothermal synthesis of $\alpha$-$Fe_2O_3$. c) XRD and d) the Raman spectra of the synthesized materials.

also show several peaks associated to $\alpha$-$Fe_2O_3$.[50,51] Finally, thermogravimetric analysis (TGA) shows that 27 wt% of the electrodes is CNTs (Figure S4c, Supporting Information), which is slightly higher than the typical 10 wt% of conductive additive. However, in this case, the CNTs also act as a high-area scaffold, and they allow for an almost binder-free operation. Finally, we demonstrate that our approach for microwave-assisted hydrothermal synthesis on VACNTs can also be used with other reactions. For example, Figure S5

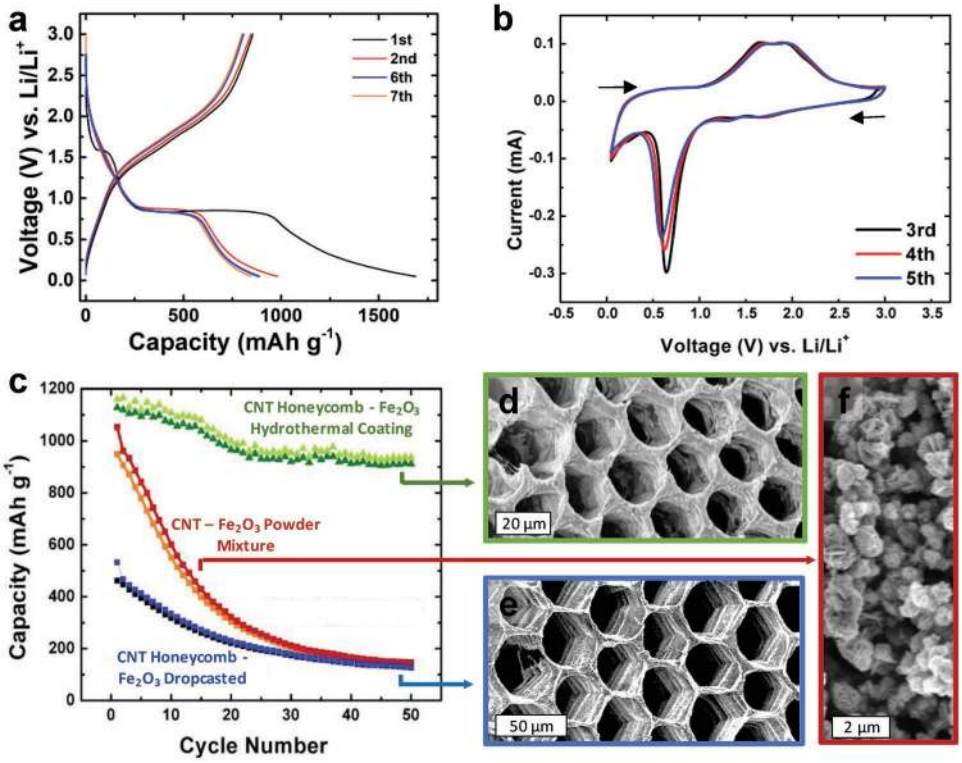


**Figure 3.** a) Charge–discharge curves and b) cyclic voltammetry of the hydrothermally synthesized CNT- $Fe_2O_3$ honeycomb electrode. c) Cycling at 0.2 C of the d) new electrode architecture, e) the same CNT honeycomb architecture with drop-casted active material, and f) a CNT-active material film casted at 100 µm.

(Supporting Information) shows a solvothermal synthesis route for $Fe_2O_3$ nanosheets,[52] which we analyzed using scanning electron microscopy (SEM) and energy-dispersive X-ray spectroscopy (EDX) (Figure S5d, Supporting Information).

Battery measurements performed in half-cell configuration are summarized in **Figure 3**. The charge–discharge curves at 0.05C (Figure 3a) have a well-defined voltage plateau at 0.75 V which agrees with the CV measurements (Figure 3b, 0.01 mV $s^{-1}$).[29] This voltage plateau corresponds to the conversion of $Fe^{3+}$ to $Fe^0$, whereas the redox current peak in the CV at 1.75 V corresponds to the oxidation reaction of $Fe^0$ to $Fe^{3+}$ (see Equation 1 in the Introduction).[31,40,42]

After ≈20 cycles, the battery capacity stabilizes at 912 mAh $g^{-1}$ (Figure 3c,d) which is close to the theoretical capacity of $\alpha$-$Fe_2O_3$ (1006 mAh $g^{-1}$),[42] and confirms that the CNTs are able to contact the active material well despite the 350 µm thickness of the electrode. This efficient electrical network results in a better utilization of the active material (see initial capacities in Figure 3c) and is also important for the stability of the electrode. In a control experiment, the same patterned VACNT forests are coated by simply drop-casting iron oxide nanoparticles in ethanol (synthesized using the same protocol) rather than using our in situ hydrothermal process. As shown in Figure 3d,e, hydrothermally coated and drop-casted electrodes look very similar under SEM. However, the latter show a rapid capacity fade which might be due to the formation of insulating a solid electrolyte interphase (SEI) layer between the CNTs and the drop-casted particles (Figure 3c and Figure S7, Supporting Information). This finding is in agreement with previous reports that show that synthesis of active materials directly on reduced graphene oxide (rGO) supports better capacity retention over cycling than physical mixtures of the same materials.[1] The better cycling stability of the honeycomb electrodes is also reflected in a higher Coulombic efficiency, which is shown in Figure S8 (Supporting Information).

As a further control experiment, a conventional battery electrode was casted from a slurry containing the same active material, PVDF as binder, and commercial CNT powder as conductive additive (80:10:10) with a thickness of 100 µm. These battery electrodes were cycled at 0.2 C for 50 cycles (Figure 3c,f) and also showed a rapid capacity decay despite having a lower areal loading (0.45 mg $cm^{-2}$) than the CNT honeycomb structure (1 mg $cm^{-2}$ average of three samples). We anticipate that the areal loading of the CNT honeycombs can be further enhanced in the future by reducing the cell size. In addition, we observed some variation in gravimetric capacity between cells, which might be due to differences in utilization of the active material and differences in the phase of the active material.

Next, the rate performance of the batteries was tested (**Figure 4**). When cycled at 1C, the electrode retains over 400 mAh $g^{-1}$, which is good given the thickness of the electrode. This is likely due to the open structure of the electrode and the good electric network provided by the CNTs. Further, we found that the battery recovers its initial capacity when reducing the rate, and can be cycled over 160 times without signs of capacity fade, whereas the control experiments show very little capacity after 40 cycles (see Figures 3c and 4). To investigate the structural stability of the electrode during cycling, a coin cell battery was opened after 40 cycles and imaged by SEM, as shown in Figure 4. The honeycomb structure is found

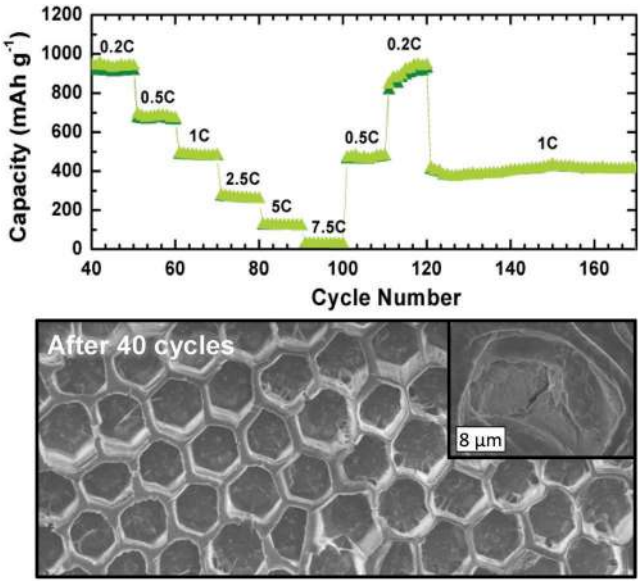


**Figure 4.** Cycling rate testing of the structured CNT-$Fe_2O_3$ electrode (upper image). Post-mortem SEM analysis of an electrode after 40 cycles (lower image).

to be maintained during cycling, which further confirms the robustness of the CNT scaffolds and novel microcontact transfer approach for binding them to the collector electrode.

## 4. Conclusion

Vertically aligned CNT forests offer a unique template for fabricating hierarchical structures with a controlled morphology at different length-scales. Unfortunately, these structures are fragile and therefore the modification of their surface chemistry or surface decoration is typically limited to gas phase processes. In this work, we have developed a combination of lithographic patterning and transfer printing which allows for microwave-assisted hydrothermal decoration of CNT forests with metal oxide nanoparticles. This process was used to coat a conversion anode material for LIBs on aligned CNT forests. This is attractive because of the high electrical conductivity and tortuosity of the CNTs as well as the good interface between the CNTs and the active battery material. In addition, manufacturing challenges such as phase segregation of the conductive additive and the active material are addressed using this process. We have fabricated 350 µm thick electrodes showing a capacity of over 900 mAh $g^{-1}$ along with a fourfold improvement in cyclability compared to CNT forests decorated by drop-casting. Finally, post-mortem analysis suggests that the developed electrode structure does not deteriorate during battery cycling.

## 5. Experimental Section

*Patterning of Catalyst for CNT Growth*: The catalyst was prepared on a silicon wafer by standard photolithography up to the resolution limit of the employed slide mask (1.8 µm). An adhesion promoter (Ti-prime), AZ 5214E positive photoresist, and AZ 351B developer were used for the photolithography. After patterning the Si wafer with photoresist, the catalyst was deposited onto the wafer using an e-beam physical vapor deposition (PVD) system (Lesker). The catalyst deposited is a 10 nm alumina ($Al_2O_3$, 1 Å $s^{-1}$), followed by a 1 nm iron layer (Fe, 0.25 Å $s^{-1}$). After the photoresist is lifted off, the catalyst is patterned.

*CNT Growth*: For the growth of VACNTs, an atmospheric pressure tube furnace was used. The standard procedure for the growth is an annealing time of 15 min under helium (100 sccm) and hydrogen (400 sccm) gas stream, then ethylene (100 sccm) was introduced. The time ethylene flows (=growth time) and the temperature of the furnace were used to control the forest height. The samples were grown at a temperature of 750 °C for 60 min. After the growth time the tube was pulled out of the furnace allowing the substrates to cool down in a helium atmosphere.

*Transfer onto PCP Film*: The PCP (PVDF, CNT, and PCBM) film was prepared following a protocol this group published previously.[21] In short, a solution of methanofullerene PCBM (15 mg), PVDF (300 mg), and CNTs (15 mg) in 6 mL dimethylformamide (DMF) was prepared, ball-milled, and drop-casted onto a glass slide. After drying, the temperature was increased to 175 °C to soften the PVDF. The grown VACNT microstructures were then transferred onto the PCP film using microcontact printing.

*α-$Fe_2O_3$ CNT Structure Synthesis*: For the synthesis of iron oxide ($Fe_2O_3$), a published protocol was modified for the use as a microwave-assisted synthesis.[29] The solution was prepared by dissolving $12.25 \times 10^{-3}$ M of iron(III) sulfate hydrate ($Fe_2(SO_4)_3 \cdot H_2O$, 244.98 g $mol^{-1}$, Fisher) in 35 mL of deionized (DI) water and 5 mL of glycerol (92.09 g $mol^{-1}$, Atom Scientific). After stirring for 10 min, the solution was transferred into teflon liners for the microwave reactor. For the VACNT structure modification, the structures on the PCP film were treated with UV–ozone (Bioforce Nanoscience) for 60 min, placed in a Teflon holder, and then slowly put into the solution. The liners were put into the microwave reactor (Multiwave Pro, Anton Paar) and heated to 165 °C for 6 h. Afterward, the electrode film was removed, the powder was filtered, and everything was washed with DI water.

*α-$Fe_2O_3$ CNT Structure Drop-Casting*: For the drop-casting of the previously synthesized iron oxide ($Fe_2O_3$) nanoparticles, these were dispersed in ethanol (7.5 mg in 1 mL) and 40 µL (=0.2 mg) were drop-casted onto the previously prepared CNT honeycomb structures on the PCP film to obtain about the same amount of active material.

*Conventional Electrode Fabrication*: For the reference electrode, microwave-synthesized iron oxide, PVDF, and CNTs in a ratio of 80:10:10 were mixed in a mortar with NMP and blade-cast (100 µm) on etched copper. The electrodes were dried in an oven at 60 °C.

*Battery Fabrication and Electrochemical Measurements*: CR 2032 type cells were assembled in an Ar filled (<0.5 ppm $H_2O$ and <0.5 $O_2$) glove box (MBraun). CNTs and iron oxide and a pure Li metal foil were used as electrodes with 1.0 M $LiPF_6$ EC/DMC (Sigma Aldrich, battery grade) as electrolyte and a Celgard as separator. The electrochemical measurements were carried out using a VMP3 Biologics multichannel potentiostat/battery cycler.

*Characterization*: SEM measurements were taken using a Leo 1530VP Gemini from Zeiss operating at an accelerating voltage of 8 keV and using an In-Lens detector. Samples were not sputtered with a metal layer. The XRD system used is a D8- B1-Gen10 Bruker XRD. Measurements were done with a step size of 0.05°(2$\theta$), and a step time of 0.5 s. The software X-Pert Highscore Plus was used for the data evaluation. Raman measurements were done using a Bruker Senterra equipment with a 532 nm laser.

## Supporting Information

Supporting Information is available from the Wiley Online Library or from the author.

## Acknowledgements

S.J. and M.D.V. acknowledge the ERC starting grant 337739-HIENA. D.C. acknowledges the Marie Skłodowska-Curie Actions MSCA-IF

660351. S.J. acknowledges the EPSRC Studentship (Hierarchical Carbon nanostructures, 1470335). S.E. acknowledges funding from EPSRC grant EP/L016087/1. S.A. and M.D.V. acknowledge the financial support from DST-UKIERI (DST/INT/UK/P-167/2017). The authors acknowledge Angelika Beinert for her help with Raman measurements.

## Conflict of Interest

The authors declare no conflict of interest.

## Keywords

carbon nanotubes, hydrothermal synthesis, Li-ion batteries, microwave-assisted synthesis

Received: March 6, 2019
Revised: August 22, 2019
Published online: September 23, 2019

[1] H. Wang, L. Cui, Y. Yang, H. S. Casalongue, *J. Am. Chem. Soc.* **2010**, *132*, 13978.
[2] H. Wang, Y. Yang, Y. Liang, L.-F. Cui, H. Sanchez Casalongue, Y. Li, G. Hong, Y. Cui, H. Dai, *Angew. Chem., Int. Ed.* **2011**, *50*, 7364.
[3] H. Wang, Y. Liang, M. Gong, Y. Li, W. Chang, T. Mefford, J. Zhou, J. Wang, T. Regier, F. Wei, H. Dai, *Nat. Commun.* **2012**, *3*, 917.
[4] H. Wang, H. Dai, *Chem. Soc. Rev.* **2013**, *42*, 3088.
[5] H. B. Wu, J. S. Chen, H. H. Hng, X. W. (David) Lou, *Nanoscale* **2012**, *4*, 2526.
[6] H. B. Wu, G. Zhang, L. Yu, X. W. (David) Lou, *Nanoscale Horiz.* **2016**, *1*, 27.
[7] H. Xia, M. Lai, L. Lu, *J. Mater. Chem.* **2010**, *20*, 6896.
[8] M. Mazloumi, S. Shadmehr, Y. Rangom, L. F. Nazar, X. (Shirley) Tang, *ACS Nano* **2013**, *7*, 4281.
[9] M. H. Modarres, J. H.-W. Lim, C. George, M. De Volder, *J. Phys. Chem. C* **2017**, *121*, 13018.
[10] C. J. Shearer, A. Cherevan, D. Eder, *Adv. Mater.* **2014**, *26*, 2295.
[11] B. Luo, Y. Fang, B. Wang, J. Zhou, H. Song, L. Zhi, *Energy Environ. Sci.* **2012**, *5*, 5226.
[12] H. Zhang, G. Cao, Y. Yang, *Energy Environ. Sci.* **2009**, *2*, 932.
[13] M. F. L. De Volder, S. H. Tawfick, R. H. Baughman, A. J. Hart, *Science* **2013**, *339*, 535.
[14] D. N. Futaba, K. Hata, T. Yamada, T. Hiraoka, Y. Hayamizu, Y. Kakudate, O. Tanaike, H. Hatori, M. Yumura, S. Iijima, *Nat. Mater.* **2006**, *5*, 987.
[15] K. L. Stano, R. Chapla, M. Carroll, J. Nowak, M. McCord, P. D. Bradford, *ACS Appl. Mater. Interfaces* **2013**, *5*, 10774.
[16] Y. Jiang, P. Wang, X. Zang, Y. Yang, A. Kozinda, L. Lin, *Nano Lett.* **2013**, *13*, 3524.
[17] J. R. Raney, H.-L. Zhang, D. E. Morse, C. Daraio, *Carbon* **2012**, *50*, 4432.
[18] K. Evanoff, J. Khan, A. A. Balandin, A. Magasinski, W. Ready, T. F. Fuller, G. Yushin, *Adv. Mater.* **2012**, *24*, 533.
[19] Y. Fan, Q. Zhang, Q. Xiao, X. Wang, K. Huang, *Carbon* **2013**, *59*, 264.
[20] W. Lu, A. Goering, L. Qu, L. Dai, *Phys. Chem. Chem. Phys.* **2012**, *14*, 12099.
[21] S. Ahmad, D. Copic, C. George, M. De Volder, *Adv. Mater.* **2016**, *28*, 6705.
[22] C. Liu, F. Li, L.-P. Ma, H.-M. Cheng, *Adv. Mater.* **2010**, *22*, E28.
[23] Y. Zhang, W. Bai, X. Cheng, J. Ren, W. Weng, P. Chen, X. Fang, Z. Zhang, H. Peng, *Angew. Chem., Int. Ed.* **2014**, *53*, 14564.
[24] H. Sun, Y. Zhang, J. Zhang, X. Sun, H. Peng, *Nat. Rev. Mater.* **2017**, *2*, 17023.
[25] M. Liao, L. Ye, Y. Zhang, T. Chen, H. Peng, *Adv. Electron. Mater.* **2019**, *5*, 1800456.
[26] S. X. Lim, S. L. Chang, F. C. Cheong, E. S. Tok, Z. Zhang, C. T. Lim, C.-H. Sow, *J. Phys. Chem. C* **2013**, *117*, 14408.
[27] P. M. Ajayan, O. Stephan, P. Redlich, C. Colliex, *Nature* **1995**, *375*, 564.
[28] M. Koo, K.-I. Park, S. H. Lee, M. Suh, D. Y. Jeon, J. W. Choi, K. Kang, K. J. Lee, *Nano Lett.* **2012**, *12*, 4810.
[29] B. Wang, J. S. Chen, H. B. Wu, Z. Wang, *J. Am. Ceram. Soc.* **2011**, *133*, 17146.
[30] L. Zhang, H. B. Wu, S. Madhavi, H. H. Hng, X. W. (David) Lou, *J. Am. Chem. Soc.* **2012**, *134*, 17388.
[31] M. V. Reddy, T. Yu, C. H. Sow, Z. X. Shen, C. T. Lim, G. V. S. Rao, B. V. R. Chowdari, *Adv. Funct. Mater.* **2007**, *17*, 2792.
[32] D. Lei, M. Zhang, B. Qu, L. Chen, Y. Wang, E. Zhang, Z. Xu, Q. Li, T. Wang, *Nanoscale* **2012**, *4*, 3422.
[33] L. Liu, Q. Weng, X. Lu, X. Sun, L. Zhang, O. G. Schmidt, *Small* **2017**, *13*, 1701847.
[34] D. Copic, S. J. Park, S. Tawfick, M. F. L. De Volder, A. J. Hart, *Lab Chip* **2011**, *11*, 1831.
[35] A. M. Schwenke, S. Hoeppener, U. S. Schubert, *Adv. Mater.* **2015**, *27*, 4113.
[36] X. Wang, X. Chen, L. Gao, H. Zheng, M. Ji, C. Tang, T. Shen, Z. Zhang, *J. Mater. Chem.* **2004**, *14*, 905.
[37] H. Liu, G. Wang, J. Park, J. Wang, H. Liu, C. Zhang, *Electrochim. Acta* **2009**, *54*, 1733.
[38] F. Cheng, W. Tang, C. Li, J. Chen, H. Liu, P. Shen, S. Dou, *Chem. - Eur. J.* **2006**, *12*, 3082.
[39] B. Koo, H. Xiong, M. D. Slater, V. B. Prakapenka, M. Balasubramanian, P. Podsiadlo, C. S. Johnson, T. Rajh, E. V. Shevchenko, *Nano Lett.* **2012**, *12*, 2429.
[40] S. Xu, C. M. Hessel, H. Ren, R. Yu, Q. Jin, M. Yang, H. Zhao, D. Wang, *Energy Environ. Sci.* **2014**, *7*, 632.
[41] Y. NuLi, R. Zeng, P. Zhang, Z. Guo, H. Liu, *J. Power Sources* **2008**, *184*, 456.
[42] P. Poizot, S. Laruelle, S. Grugeon, L. Dupont, J.-M. Tarascon, *Nature* **2000**, *407*, 496.
[43] Z. Wang, W. Zhang, X. Li, L. Gao, *J. Mater. Res.* **2016**, *31*, 1648.
[44] D. B. Mawhinney, V. Naumenko, A. Kuznetsova, J. T. Yates, J. Liu, R. E. Smalley. *J. Am. Chem. Soc.* **2000**, *122*, 2383.
[45] J. M. Simmons, B. M. Nichols, S. E. Baker, M. S. Marcus, O. M. Castellini, C.-S. Lee, R. J. Hamers, M. A. Eriksson, *J. Phys. Chem. B* **2006**, *110*, 7113.
[46] S. Tawfick, M. De Volder, D. Copic, S. J. Park, C. Oliver, E. S. Polsen, M. J. Roberts, A. J. Hart, *Adv. Mater.* **2012**, *24*, 1628.
[47] S. Tawfick, Z. Zhao, M. Maschmann, A. Brieland-Shoultz, M. De Volder, J. W. Baur, W. Lu, A. J. Hart, *Langmuir* **2013**, *29*, 5190.
[48] M. De Volder, S. H. Tawfick, S. J. Park, D. Copic, Z. Zhao, W. Lu, A. J. Hart, *Adv. Mater.* **2010**, *22*, 4384.
[49] F. Pourfayaz, Y. Mortazavi, A.-A. Khodadadi, S. H. Jafari, S. Boroun, M. V. Naseh, *Appl. Surf. Sci.* **2014**, *295*, 66.
[50] D. Bersani, P. P. Lottici, A. Montenero, *J. Raman Spectrosc.* **1999**, *30*, 355.
[51] I. R. Beattie, T. R. Gilson, *J. Chem. Soc. A* **1970**, 980.
[52] L. Li, H. B. Wu, L. Yu, S. Madhavi, X. W. D. Lou, *Adv. Mater. Interfaces* **2014**, *1*, 1400050.